SCIENCE CHINA
Information Sciences

• Supplementary File •

Supplementary Information

Giant orbit-to-charge conversion induced via the inverse orbital Hall effect

Renyou Xu,[1,2] Hui Zhang,[1,a)] Yuhao Jiang,[1] Houyi Cheng,[1,2] Yunfei Xie,[3] Yuxuan Yao,[1] Danrong Xiong,[1] Zhaozhao Zhu,[4,5] Xiaobai Ning,[1] Runze Chen,[1] Yan Huang,[1] Ao Du,[1] Shijie Xu,[1,2] Jianwang Cai,[4] Yong Xu,[1,2] Tao Liu,[3] Jirong Sun,[4,5] Weisheng Zhao[1,,2,a)]

AFFILIATIONS

[1]Fert Beijing Institute, School of Integrated Circuit Science and Engineering, Beihang University, Beijing 100191, China

[2]Hefei Innovation Research Institute, Beihang University, Hefei 230013, China

[3]National Engineering Research Center of Electromagnetic Radiation Control Materials, University of Electronic Science and Technology of China, Chengdu 610054, China

[4]Beijing National Laboratory for Condensed Matter Physics, Institute of Physics, Chinese Academy of Sciences, Beijing 100190, China

[5]Songshan Lake Materials Laboratory, Dongguan, Guangdong 523808, China

[a)]Authors to whom correspondence should be addressed: huizh@buaa.edu.cn; and weisheng.zhao@buaa.edu.cn

Table of Contents

S1. Theoretical modeling

The well-known SSE and SP, enable the injection of spin current from the FM layer into the adjacent NM layer[1]. This injected spin current undergoes diffusion and is converted into a charge current via the ISHE in the NM layer. However, existing models of spin transport and spin-to-charge conversion may not be directly applicable to scenarios involving the IOHE[2,3]. Recent studies have revealed that in transition metals, spin current is often accompanied by orbital current during transport processes[4-6]. As shown in FIG.S1.(a) the IOHE and ISHE in a ferromagnet/conversion-material (CM) bilayer are described by taking into account both SAM and OAM diffusion.

As the spin current (red arrow) is injected from the FM layer into the adjacent CM layer, it not only undergoes spin-to-charge conversion via the ISHE, but also generates an additional orbital current (blue arrow) through spin-to-orbit conversion[6,7]. This process is believed to arise from spin diffusion under the influence of strong SOC in the CM layer[8]. The OAM dynamics along the spin current injection direction (i.e., the *z*-axis) is given by:

$$j_L(z) = -\frac{\sigma_{\mathrm{CM}}}{2e}\frac{d\mu_L}{dz}, \tag{1}$$

$$\frac{d^2\mu_L}{dz^2} = \frac{\mu_L}{\lambda_L^2} - \frac{\mu_S}{\lambda_{LS}^2}, \tag{2}$$

where σ_{CM} is the electrical conductivity of the CM layer, e is the elementary charge. μ_S and μ_L are the spin and orbital chemical potentials, respectively. Equation (2) captures the generation and relaxation of the orbital chemical potential: the first term describes orbital relaxation, while the second term accounts for spin-to-orbit conversion, with a rate proportional to μ_S [9]. The parameters λ_L, and λ_{LS} represent the orbital diffusion length, and the coupling length, respectively, with λ_{LS} defining both the strength and characteristic length scale of SOC-induced spin–orbital interconversion.

The orbital current can also be converted into a charge current via IOHE , in a process analogous to ISHE. The charge current generated via ISHE or IOHE can be expressed as:

$$I_{\mathrm{ISHE(IOHE)}}^{\mathrm{CM}} = \int_0^{t_{\mathrm{CM}}} j_c(z)dz = -\sigma_{\mathrm{SH(OH)}}^{\mathrm{CM}} \times \mu_{S(L)}^{\mathrm{CM}}\Big|_0^{t_{\mathrm{CM}}}, \tag{3}$$

where $j_c(z)$ is the charge current density, $\sigma_{\mathrm{SH(OH)}}^{\mathrm{CM}}$ is the spin (orbital) Hall conductivity (SHC/OHC) of the CM layer, and t_{CM} is the thickness of the CM layer. We note that in the FM/CM bilayer system, ISHE and IOHE coexist and are inherently coupled within the CM layer, making it difficult to separate their respective contributions.

To further investigate the IOHE, we introduce an additional NM layer, as illustrated in FIG.S1.(b) When the CM thickness is smaller than its spin and orbital diffusion lengths, SAM and OAM do not fully relax within the CM, thus allowing both spin and orbital currents to be injected into the adjacent NM layer. As a result, additional ISHE and IOHE contributions arise in the NM layer.

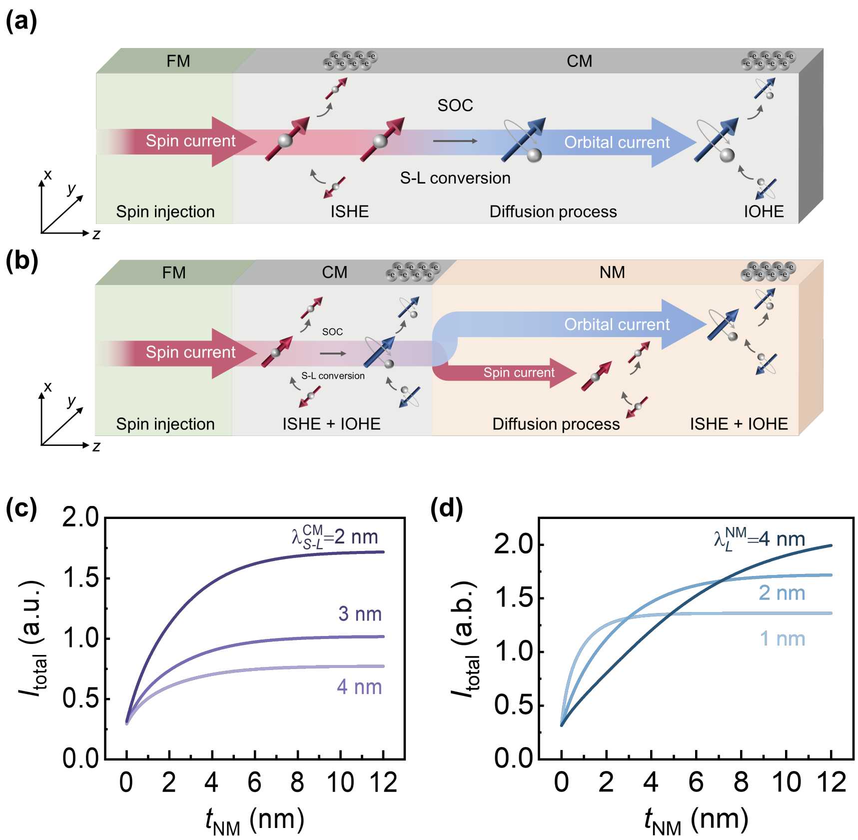

FIG.S1. Modeling of spin–orbit transport and orbit-to-charge conversion in FM/CM(/NM) heterostructures. Schematic illustration of ISHE and IOHE, considering both spin and orbital transport process in a) An FM/CM bilayer sample and b) an FM/CM/NM trilayer sample. c) The total charge current as a function of the NM layer thickness for different SOC lengths, $\lambda_{S-L}^{\mathrm{CM}} = 2$, 3 and 4 nm. d) The total charge current as a function of the NM layer thickness for different orbital diffusion lengths, $\lambda_L^{\mathrm{CM}} = 1, 2$,and 4 nm.

Our model considers the NM layer to be a light metal with negligible SOC, implying that interconversion between SAM and OAM is negligible, and that the SHC is at least one order of magnitude smaller than the OHC [10]. Under these conditions, spin and orbital diffusion can be treated independently, and the IOHE is assumed to dominate over the ISHE in the NM layer due to the significantly larger OHC. The total charge current from both the CM and NM layers can then be expressed as:

$$I_{total} = -(\sigma_{\mathrm{SH}}^{\mathrm{CM}} \times \mu_S^{\mathrm{CM}}\Big|_0^{t_{\mathrm{CM}}} + \sigma_{\mathrm{OH}}^{\mathrm{CM}} \times \mu_L^{\mathrm{CM}}\Big|_0^{t_{\mathrm{CM}}} + \sigma_{\mathrm{SH}}^{\mathrm{NM}} \times \mu_S^{\mathrm{NM}}\Big|_{t_{\mathrm{CM}}}^{t_{\mathrm{NM}}} + \sigma_{\mathrm{OH}}^{\mathrm{NM}} \times \mu_L^{\mathrm{NM}}\Big|_{t_{\mathrm{CM}}}^{t_{\mathrm{NM}}}), \quad (4)$$

where $z = 0$, t_{CM}, and t_{NM} correspond to the FM/CM, CM/NM, and NM/vacuum interfaces, respectively. See Supplementary Note S1 for additional derivation and boundary conditions.

We apply our model to analyze ISHE and IOHE in an FM/CM/NM trilayer system. Since our primary interest lies in the IOHE contribution, we calculate I_{total} as a function of NM thickness, focusing on two key parameters.

First, the coupling length $\lambda_{S-L}^{\mathrm{CM}}$, which governs the efficiency of spin-to-orbit conversion in the CM layer. As shown in FIG.S1.(c), the total current I_{total} increases with NM thickness and tends to saturate at larger thicknesses. The amplitude and saturation level of I_{total} increase with decreasing $\lambda_{S-L}^{\mathrm{CM}}$. A shorter $\lambda_{S-L}^{\mathrm{CM}}$ indicates stronger SOC, leading to more OAM generation in the CM layer during the SAM diffusion process. The enhanced OAM can be converted into charge current in both the CM and NM layers, resulting in a higher I_{total}. Therefore, a CM layer with stronger SOC is beneficial for achieving higher signal levels and for studying the IOHE process.

Second, the orbital diffusion length in the NM layer, λ_L^{NM}, denotes the characteristic length over which the orbital chemical potential decays due to relaxation processes. As shown in FIG.S1.(d), when λ_L^{NM} is short, I_{total} increases rapidly at small NM thicknesses but saturates quickly due to limited orbital transport. In contrast, a larger λ_L^{NM} allows OAM to penetrate deeper into the NM layer, leading to saturation at a larger thickness and with a higher amplitude. This behavior is analogous to the spin diffusion process [11].

For completeness, we now give the detailed derivation of the coupled spin–orbital diffusion model used to analyze the FM/CM/NM trilayer. We begin with the spin and orbital transport equations in a single NM layer, and then generalize the formalism to the CM layer by including spin-to-orbit conversion. Together with appropriate boundary conditions at the FM/CM and CM/NM interfaces, this treatment yields an explicit expression for the total inverse charge current generated by ISHE and IOHE. The resulting model is used to fit the thickness-dependent SSE and SP data presented in the main text.

We note that the SSE/SP signal arises from the inverse spin Hall effect (ISHE) and the inverse orbital Hall effect (IOHE) occurring in both the conversion-material (CM) and nonmagnetic material (NM) layers. In order to quantify these contributions, we utilized a one-dimensional spin-orbital diffusion model based on previous research [9,12,13]

Initially, we focused on a single nonmagnetic layer where a spin/orbital current is injected along the z-direction, inducing ISHE/IOHE. The diffusion of spins and orbitals in the NM layer can be described by the following equations:

$$\frac{d^2\mu_S}{dz^2} = \frac{\mu_S}{\lambda_S^2}, \tag{5}$$

$$\frac{d^2\mu_L}{dz^2} = \frac{\mu_L}{\lambda_L^2}, \tag{6}$$

$$j_S(y) = -\frac{\sigma_{\mathrm{NM}}}{2e}\frac{d\mu_S}{dz}, \tag{7}$$

$$j_L(y) = -\frac{\sigma_{\mathrm{NM}}}{2e}\frac{d\mu_L}{dz}, \tag{8}$$

Here, μ_S, μ_L, λ_S, λ_L, σ_{NM}, j_S, and j_L are spin chemical potential, orbital chemical potential, spin diffusion length, orbital diffusion length, current conductivity of the NM layer, *z*-dependent spin current density, and *z*-dependent orbital current density, respectively. It should be noted that the spin-orbit coupling (SOC) strength of NM is significantly weaker than that of CM [14]. Therefore, we assume that the transport of spin and orbital angular momentum is independent and neglects the interconversion between spin and orbital in the NM layer. The solutions to equations (5) and (6) can be expressed as:

$$\mu_S = A'_1 e^{\frac{z}{\lambda_S}} + A'_2 e^{-\frac{z}{\lambda_S}}, \tag{9}$$

$$\mu_L = B'_1 e^{\frac{z}{\lambda_L}} + B'_2 e^{-\frac{z}{\lambda_L}}. \tag{10}$$

To simplify subsequent calculations, we write the expression in the following form

$$\mu_S = A_1 \cosh\left(\frac{z}{\lambda_S}\right) + A_2\lambda_S \sinh\,(\frac{z}{\lambda_S}), \tag{11}$$

$$\mu_L = B_1 \cosh\left(\frac{z}{\lambda_L}\right) + B_2\lambda_L \sinh\left(\frac{z}{\lambda_L}\right), \tag{12}$$

the coefficients A and B can be determined by applying the appropriate boundary conditions.

Regarding the CM layer, we introduce a spin-to-orbit conversion term in equation (12), and the diffusion of spins and orbitals in the CM layer can be described as follows:

$$\frac{d^2\mu_S}{dz^2} = \frac{\mu_S}{\lambda_S^2}, \tag{13}$$

$$\frac{d^2\mu_L}{dz^2} = \frac{\mu_L}{\lambda_L^2} - \frac{\mu_S}{\lambda_{LS}^2}, \tag{14}$$

$$j_S(z) = -\frac{\sigma_{\mathrm{CM}}}{2e}\frac{d\mu_S}{dz}, \tag{15}$$

$$j_L(z) = -\frac{\sigma_{\mathrm{CM}}}{2e}\frac{d\mu_L}{dz}. \tag{16}$$

Here, σ_{CM} represents the current conductivity of the CM layer, and λ_{LS} is the effective transformation length for spin-orbital interconversion. A higher λ_{LS} indicates that the system requires a longer propagation distance for spin-orbit transformation. The second term on the right side of equation (14) describes the conversion of spin current to orbital current as the orbital current diffuses in the Pt layer. To solve the coupled equations (11) and (12), we obtain the following expressions:

$$\mu_S = C_1 \cosh\left(\frac{z}{\lambda_S}\right) + C_2\lambda_S \sinh\left(\frac{z}{\lambda_S}\right), \tag{17}$$

$$\begin{aligned}\mu_L = -C_0\left\{C_1\left[\cosh\left(\frac{z}{\lambda_S}\right) - \cosh\left(\frac{z}{\lambda_L}\right)\right] + C_2\left[\lambda_S\sinh\left(\frac{z}{\lambda_S}\right) - \lambda_L\sinh\left(\frac{z}{\lambda_L}\right)\right]\right\}\\ +C_3 \cosh\left(\frac{z}{\lambda_L}\right) + C_4\,\lambda_L\sinh\left(\frac{z}{\lambda_L}\right),\end{aligned} \tag{18}$$

where $C_0 = (\lambda_L\lambda_S)^2/(\lambda_L^2 - \lambda_S^2)\lambda_{LS}^2$ is a coefficient for the conversion efficiency between spin and orbital.

Now we have derived the expression for μ_S and μ_L in the single CM and NM layers, we can discuss the boundary conditions in the FM/CM/NM trilayer to determine the coefficients for the NM layer ($A_1, A_2, B_1, and\ B_2$) and for the CM layer ($C_1, C_2, C_3, and\ C_4$).

In the measurements of the SSE in the YIG/Pt/Ru trilayer, we make the assumption that the FM layer injects a constant spin current ($J_{S,init} = J_{S0}$) and a constant orbital current ($J_{L,init} = 0$) into the CM layer at $z = -d_{CM}$ while applying a constant temperature gradient along the z-direction

$$\begin{cases} -\dfrac{\sigma_{\mathrm{CM}}}{2e}\dfrac{C_1}{\lambda_S^{\mathrm{CM}}}\sinh\left(\dfrac{-d_{\mathrm{CM}}}{\lambda_S^{\mathrm{CM}}}\right) - \dfrac{\sigma_{\mathrm{CM}}}{2e}C_2\cosh\left(\dfrac{-d_{\mathrm{CM}}}{\lambda_S^{\mathrm{CM}}}\right) = J_{S0}, \\ C_0\dfrac{\sigma_{\mathrm{CM}}}{2e}\left(\dfrac{C_1}{\lambda_S^{\mathrm{CM}}}\sinh\left(\dfrac{-d_{\mathrm{CM}}}{\lambda_S^{\mathrm{CM}}}\right) - \dfrac{C_1}{\lambda_L^{\mathrm{CM}}}\sinh\left(\dfrac{-d_{\mathrm{CM}}}{\lambda_L^{\mathrm{CM}}}\right) + C_2\cosh\left(\dfrac{-d_{\mathrm{CM}}}{\lambda_S^{\mathrm{CM}}}\right) - C_2\cosh\left(\dfrac{-d_{\mathrm{CM}}}{\lambda_L^{\mathrm{CM}}}\right)\right) \\ -\dfrac{\sigma_{\mathrm{CM}}}{2e}\dfrac{C_3}{\lambda_L^{\mathrm{CM}}}\sinh\left(\dfrac{-d_{\mathrm{CM}}}{\lambda_L^{\mathrm{CM}}}\right) - \dfrac{\sigma_{\mathrm{CM}}}{2e}C_4\cosh\left(\dfrac{-d_{\mathrm{CM}}}{\lambda_L^{\mathrm{CM}}}\right) = 0. \end{cases} \tag{19}$$

To justify the boundary condition $J_{L,init} = 0$, we note that although direct orbital angular momentum pumping from magnetic insulators has been reported in materials with strong spin–orbit coupling, the corresponding contribution is expected to be much weaker in YIG-based heterostructures. In particular, previous experiments have shown that the SSE signal in FM/CM bilayers is negligibly small compared to that in trilayer structures with an additional heavy-metal layer, indicating that the directly injected orbital current at the FM/CM interface is much smaller than the injected spin current [5]. Therefore, the orbital current responsible for the orbital-to-charge conversion in Ru is predominantly generated via spin–orbit coupling in the Pt layer, rather than being directly injected from YIG. Under this consideration, neglecting direct OAM injection at the FM/CM interface constitutes a reasonable approximation for describing the dominant mechanism in our experiments.This assumption is supported by experimental observations where the FM/CM bilayer exhibits a negligible SSE signal [15]. Due to the significantly stronger injected spin current than the orbital current, and the relatively thin CM layer, the generated spin current resulting from orbit-to-spin conversion is much smaller than the injected spin current. As a result, we focus on the spin-to-orbit conversion while neglecting the orbit-to-spin conversion in the CM layer. To achieve a steady-state condition and reduce the number of free parameters in the fitting process, we neglect the loss of the spin (orbital) current when it passes through the interface, assume that the spin (orbital) chemical potential and the spin (orbital) current are continuous at the interface of the CM/NM bilayer, where the z-coordinate is 0 for both CM and NM layer, so the formula can be simplified as follows:

$$\begin{cases} A_1 = C_1, \\ B_1 = C_3, \\ -\dfrac{\sigma_{\mathrm{NM}}}{2e} A_2 = -\dfrac{\sigma_{\mathrm{NM}}}{2e} C_2, \\ -\dfrac{\sigma_{\mathrm{NM}}}{2e} B_2 = -\dfrac{\sigma_{\mathrm{NM}}}{2e} C_4, \end{cases} \tag{20}$$

Additionally, we impose the condition that the spin (orbital) current vanishes at the edge of the NM layer ($z = d_{\mathrm{NM}}$).

$$\begin{cases} -\dfrac{\sigma_{\mathrm{NM}}}{2e} \dfrac{A_1}{\lambda_S^{\mathrm{NM}}} \sinh\left(\dfrac{d_{\mathrm{NM}}}{\lambda_S^{\mathrm{NM}}}\right) - \dfrac{\sigma_{\mathrm{NM}}}{2e} A_2 \cosh\left(\dfrac{d_{\mathrm{NM}}}{\lambda_S^{\mathrm{NM}}}\right) = 0, \\ -\dfrac{\sigma_{\mathrm{NM}}}{2e} \dfrac{B_1}{\lambda_L^{\mathrm{NM}}} \sinh\left(\dfrac{d_{\mathrm{NM}}}{\lambda_L^{\mathrm{NM}}}\right) - \dfrac{\sigma_{\mathrm{NM}}}{2e} B_2 \cosh\left(\dfrac{d_{\mathrm{NM}}}{\lambda_L^{NM}}\right) = 0, \end{cases} \tag{21}$$

By applying these boundary conditions, we can solve equations (9), (10), (15), and (16) to determine the distribution of the spin and orbital chemical potentials along the z-direction in the FM/CM/NM system. We can obtain

$$C_1 = \frac{2eJ_{S0}}{\cosh\left(\dfrac{d_{\mathrm{CM}}}{\lambda_S^{\mathrm{CM}}}\right)} \left(\frac{\sigma_{\mathrm{CM}}}{\lambda_S^{\mathrm{CM}}} \tanh\left(\frac{d_{\mathrm{CM}}}{\lambda_S^{\mathrm{CM}}}\right) + \frac{\sigma_{\mathrm{NM}}}{\lambda_S^{\mathrm{NM}}} \tanh\left(\frac{d_{\mathrm{NM}}}{\lambda_S^{\mathrm{NM}}}\right)\right)^{-1}, \tag{22}$$

$$C_2 = -\frac{\sigma_{\mathrm{NM}}}{\sigma_{\mathrm{CM}}} \frac{2eJ_{S0} \tanh\left(\dfrac{d_{\mathrm{NM}}}{\lambda_S^{\mathrm{NM}}}\right)}{\lambda_S^{\mathrm{NM}} \cosh\left(\dfrac{d_{\mathrm{CM}}}{\lambda_S^{\mathrm{CM}}}\right)} \left(\frac{\sigma_{\mathrm{CM}}}{\lambda_S^{\mathrm{CM}}} \tanh\left(\frac{d_{\mathrm{CM}}}{\lambda_S^{\mathrm{CM}}}\right) + \frac{\sigma_{\mathrm{NM}}}{\lambda_S^{\mathrm{NM}}} \tanh\left(\frac{d_{\mathrm{NM}}}{\lambda_S^{\mathrm{NM}}}\right)\right)^{-1}, \tag{23}$$

$$C_3 = C_0 \left(1 - \frac{\left(\dfrac{\sigma_{\mathrm{CM}}}{\lambda_L^{\mathrm{CM}}} \tanh\left(\dfrac{d_{\mathrm{CM}}}{\lambda_L^{\mathrm{CM}}}\right) + \dfrac{\sigma_{\mathrm{NM}}}{\lambda_S^{\mathrm{NM}}} \tanh\left(\dfrac{d_{\mathrm{NM}}}{\lambda_S^{\mathrm{NM}}}\right)\right) \cosh\left(\dfrac{d_{\mathrm{NM}}}{\lambda_L^{\mathrm{CM}}}\right)}{\left(\dfrac{\sigma_{\mathrm{CM}}}{\lambda_S^{\mathrm{CM}}} \tanh\left(\dfrac{d_{\mathrm{CM}}}{\lambda_S^{\mathrm{CM}}}\right) + \dfrac{\sigma_{\mathrm{NM}}}{\lambda_S^{\mathrm{NM}}} \tanh\left(\dfrac{d_{\mathrm{NM}}}{\lambda_S^{\mathrm{NM}}}\right)\right) \cosh\left(\dfrac{d_{\mathrm{NM}}}{\lambda_S^{\mathrm{CM}}}\right)} \right)$$

$$\frac{2eJ_{S0}}{\cosh\left(\frac{d_{\mathrm{CM}}}{\lambda_L^{\mathrm{CM}}}\right)}\left(\frac{\sigma_{\mathrm{CM}}}{\lambda_L^{\mathrm{CM}}}\tanh\left(\frac{d_{\mathrm{CM}}}{\lambda_L^{\mathrm{CM}}}\right)+\frac{\sigma_{\mathrm{NM}}}{\lambda_L^{\mathrm{NM}}}\tanh\left(\frac{d_{\mathrm{NM}}}{\lambda_L^{\mathrm{NM}}}\right)\right)^{-1}, \tag{24}$$

$$C_4=-\frac{\sigma_{\mathrm{NM}}}{\sigma_{\mathrm{CM}}}C_0\left(1-\frac{\left(\frac{\sigma_{\mathrm{CM}}}{\lambda_L^{\mathrm{CM}}}\tanh\left(\frac{d_{\mathrm{CM}}}{\lambda_L^{\mathrm{CM}}}\right)+\frac{\sigma_{\mathrm{NM}}}{\lambda_S^{\mathrm{NM}}}\tanh\left(\frac{d_{\mathrm{NM}}}{\lambda_S^{\mathrm{NM}}}\right)\right)\cosh\left(\frac{d_{\mathrm{CM}}}{\lambda_L^{\mathrm{CM}}}\right)}{\left(\frac{\sigma_{\mathrm{CM}}}{\lambda_S^{\mathrm{CM}}}\tanh\left(\frac{d_{\mathrm{CM}}}{\lambda_S^{\mathrm{CM}}}\right)+\frac{\sigma_{\mathrm{NM}}}{\lambda_S^{\mathrm{NM}}}\tanh\left(\frac{d_{\mathrm{NM}}}{\lambda_S^{\mathrm{NM}}}\right)\right)\cosh\left(\frac{d_{\mathrm{CM}}}{\lambda_S^{\mathrm{CM}}}\right)}\right)$$
$$\frac{2eJ_{S0}\tanh\left(\frac{d_{\mathrm{NM}}}{\lambda_L^{\mathrm{NM}}}\right)}{\lambda_L^{\mathrm{NM}}\cosh\left(\frac{d_{\mathrm{CM}}}{\lambda_L^{\mathrm{CM}}}\right)}\left(\frac{\sigma_{\mathrm{CM}}}{\lambda_L^{\mathrm{CM}}}\tanh\left(\frac{d_{\mathrm{CM}}}{\lambda_L^{\mathrm{NM}}}\right)+\frac{\sigma_{\mathrm{NM}}}{\lambda_L^{\mathrm{NM}}}\tanh\left(\frac{d_{\mathrm{NM}}}{\lambda_L^{\mathrm{NM}}}\right)\right)^{-1}, \tag{25}$$

and

$$A_1=\frac{2eJ_{S0}}{\cosh\left(\frac{d_{\mathrm{CM}}}{\lambda_S^{\mathrm{CM}}}\right)}\left(\frac{\sigma_{\mathrm{CM}}}{\lambda_S^{\mathrm{CM}}}\tanh\left(\frac{d_{\mathrm{CM}}}{\lambda_S^{\mathrm{CM}}}\right)+\frac{\sigma_{\mathrm{NM}}}{\lambda_S^{\mathrm{NM}}}\tanh\left(\frac{d_{\mathrm{NM}}}{\lambda_S^{\mathrm{NM}}}\right)\right)^{-1}, \tag{26}$$

$$A_2=-\frac{2eJ_{S0}\tanh\left(\frac{d_{\mathrm{NM}}}{\lambda_S^{\mathrm{NM}}}\right)}{\lambda_S^{\mathrm{NM}}\cosh\left(\frac{d_{\mathrm{CM}}}{\lambda_S^{\mathrm{CM}}}\right)}\left(\frac{\sigma_{\mathrm{CM}}}{\lambda_S^{\mathrm{CM}}}\tanh\left(\frac{d_{\mathrm{CM}}}{\lambda_S^{\mathrm{CM}}}\right)+\frac{\sigma_{\mathrm{NM}}}{\lambda_S^{\mathrm{NM}}}\tanh\left(\frac{d_{\mathrm{NM}}}{\lambda_S^{\mathrm{NM}}}\right)\right)^{-1}, \tag{27}$$

$$B_1=C_0\left(1-\frac{\left(\frac{\sigma_{\mathrm{CM}}}{\lambda_L^{\mathrm{CM}}}\tanh\left(\frac{d_{\mathrm{CM}}}{\lambda_L^{\mathrm{CM}}}\right)+\frac{\sigma_{\mathrm{NM}}}{\lambda_S^{\mathrm{NM}}}\tanh\left(\frac{d_{\mathrm{NM}}}{\lambda_S^{\mathrm{NM}}}\right)\right)\cosh\left(\frac{d_{\mathrm{CM}}}{\lambda_L^{\mathrm{CM}}}\right)}{\left(\frac{\sigma_{\mathrm{CM}}}{\lambda_S^{\mathrm{CM}}}\tanh\left(\frac{d_{\mathrm{CM}}}{\lambda_S^{\mathrm{CM}}}\right)+\frac{\sigma_{\mathrm{NM}}}{\lambda_S^{\mathrm{NM}}}\tanh\left(\frac{d_{\mathrm{NM}}}{\lambda_S^{\mathrm{NM}}}\right)\right)\cosh\left(\frac{d_{\mathrm{CM}}}{\lambda_S^{\mathrm{CM}}}\right)}\right)$$
$$\frac{2eJ_{S0}}{\cosh\left(\frac{d_{\mathrm{CM}}}{\lambda_{\mathrm{L}}^{CM}}\right)}\left(\frac{\sigma_{\mathrm{CM}}}{\lambda_L^{CM}}\tanh\left(\frac{d_{\mathrm{CM}}}{\lambda_L^{\mathrm{CM}}}\right)+\frac{\sigma_{\mathrm{NM}}}{\lambda_L^{\mathrm{NM}}}\tanh\left(\frac{d_{\mathrm{NM}}}{\lambda_L^{\mathrm{NM}}}\right)\right)^{-1}, \tag{28}$$

$$B_2=-C_0\left(1-\frac{\left(\frac{\sigma_{\mathrm{CM}}}{\lambda_L^{\mathrm{CM}}}\tanh\left(\frac{d_{\mathrm{CM}}}{\lambda_L^{\mathrm{CM}}}\right)+\frac{\sigma_{\mathrm{NM}}}{\lambda_S^{\mathrm{NM}}}\tanh\left(\frac{d_{\mathrm{NM}}}{\lambda_S^{\mathrm{NM}}}\right)\right)\cosh\left(\frac{d_{\mathrm{CM}}}{\lambda_L^{\mathrm{CM}}}\right)}{\left(\frac{\sigma_{\mathrm{CM}}}{\lambda_S^{\mathrm{CM}}}\tanh\left(\frac{d_{\mathrm{CM}}}{\lambda_S^{\mathrm{CM}}}\right)+\frac{\sigma_{\mathrm{NM}}}{\lambda_S^{\mathrm{NM}}}\tanh\left(\frac{d_{\mathrm{NM}}}{\lambda_S^{\mathrm{NM}}}\right)\right)\cosh\left(\frac{d_{\mathrm{CM}}}{\lambda_S^{\mathrm{CM}}}\right)}\right)$$
$$\frac{2eJ_{S0}\tanh\left(\frac{d_{\mathrm{NM}}}{\lambda_L^{\mathrm{NM}}}\right)}{\lambda_L^{\mathrm{NM}}\cosh\left(\frac{d_{\mathrm{CM}}}{\lambda_L^{\mathrm{CM}}}\right)}\left(\frac{\sigma_{\mathrm{CM}}}{\lambda_L^{\mathrm{CM}}}\tanh\left(\frac{d_{CM}}{\lambda_L^{\mathrm{CM}}}\right)+\frac{\sigma_{\mathrm{NM}}}{\lambda_L^{\mathrm{NM}}}\tanh\left(\frac{d_{\mathrm{NM}}}{\lambda_L^{\mathrm{NM}}}\right)\right)^{-1}, \tag{29}$$

This allows us to investigate the behavior and characteristics of the spin and orbital dynamics within the trilayer structure.

The inverse charge current density resulting from the ISHE and IOHE can be expressed as:

$$j_C=\theta_{\mathrm{SH(OH)}}\frac{2e}{\hbar}j_{S(L)}, \tag{30}$$

where the $\theta_{\mathrm{SH(OH)}}$ is the spin (orbital) Hall angle. By substituting equations (7), (8), (15), and (16) into equation (30), we can rewrite it as:

$$j_{C1}=-\sigma_{\mathrm{SH}}^{\mathrm{NM}}\frac{d\mu_S}{dz}, \tag{31}$$

$$j_{C2} = -\sigma_{\mathrm{OH}}^{\mathrm{NM}} \frac{d\mu_L}{dz}, \tag{32}$$

$$j_{C3} = -\sigma_{\mathrm{SH}}^{\mathrm{CM}} \frac{d\mu_S}{dz}, \tag{33}$$

$$j_{C4} = -\sigma_{\mathrm{OH}}^{\mathrm{CM}} \frac{d\mu_L}{dz}, \tag{34}$$

By Integrating equations (31), (32), (33), and (34) along the *z*-direction, we can obtain the total inverse charge current resulting from the ISHE and IOHE occurring in both the CM layer and the NM layer:

$$I_{total} = -\left(\sigma_{\mathrm{SH}}^{\mathrm{CM}} \times \mu_S^{\mathrm{CM}}\Big|_0^{t_{\mathrm{CM}}} + \sigma_{\mathrm{OH}}^{\mathrm{CM}} \times \mu_L^{\mathrm{CM}}\Big|_0^{t_{\mathrm{CM}}} + \sigma_{\mathrm{SH}}^{\mathrm{NM}} \times \mu_S^{\mathrm{NM}}\Big|_{t_{\mathrm{CM}}}^{t_{\mathrm{CM}}+t_{\mathrm{NM}}} + \sigma_{\mathrm{OH}}^{\mathrm{NM}} \times \mu_L^{\mathrm{NM}}\Big|_{t_{\mathrm{CM}}}^{t_{\mathrm{CM}}+t_{\mathrm{NM}}}\right), \tag{35}$$

where, σ_{SH}, σ_{OH}, μ_S, and μ_L are the spin Hall conductivity, orbital Hall conductivity, spin chemical potential, and orbital chemical potential with their superscripts indicating the corresponding elements (CM or NM). Hence, the total signal generated by the FM/CM/NM system can be expressed in terms of the spin (orbital) chemical potential as a function of the NM layer thickness.

We adopt $\sigma_{\mathrm{SHE}}^{\mathrm{Pt}} = 2000\ \hbar/\mathrm{e}(\Omega \cdot \mathrm{m})^{-1}$, $\sigma_{\mathrm{OHE}}^{\mathrm{Pt}} = 4000\ \hbar/\mathrm{e}(\Omega \cdot \mathrm{m})^{-1}$, $\sigma_{\mathrm{SHE}}^{\mathrm{Ru}} = 100\ \hbar/\mathrm{e}(\Omega \cdot \mathrm{m})^{-1}$, and $\sigma_{\mathrm{OHE}}^{\mathrm{Ru}} = 9000\ \hbar/\mathrm{e}(\Omega \cdot \mathrm{m})^{-1}$ from previous work [10] and the parameters used for fitting the experimental results can be found in Table I, which are similar to those obtained in previous works [10,16,17].

We adopt the same boundary condition for SSE and SP fitting. Although the spin current is driven by RF magnetic field in SP measurement, it's also reasonable to assume a constant spin/orbital current ($J_S = J_{S0}$, $J_L = 0$) injected from the YIG layer to the Pt layer [1], when varying the thickness of the Ru layer in YIG/Pt/Ru trilayer system. As a result, expression can also be used to fit the SP results as shown in Table I.

Table. S1 Parameters used to fit the SSE/SP signal in the thickness dependence of the Ru layer in the YIG/Pt/Ru trilayer.

	λ_s (nm)		λ_l (nm)		λ_{ls} (nm)	
	SSE	SP	SSE	SP	SSE	SP
Ru	6.5	5.3	1.9	1.9	-	-
Pt	2.7	3.1	3.3	3.3	2.45	2.4

S2. Thin film deposition and characterization

YIG thin film was firstly deposited on a (111)-oriented gadolinium gallium garnet (GGG) substrate. Before depositing the sequential multilayers, the GGG/YIG samples underwent a post-annealing process in an oxygen atmosphere at 800°C for two hours, which is considered a crucial step in preparing high-quality heterostructure. After the annealing process, the GGG/YIG film was transferred back to the magnetron sputter chamber to deposit the subsequent layers. All the metal/insulating layers were deposited using DC/RF magnetron sputter with the base pressure of the magnetron sputter chamber below 10^{-9} mbar.

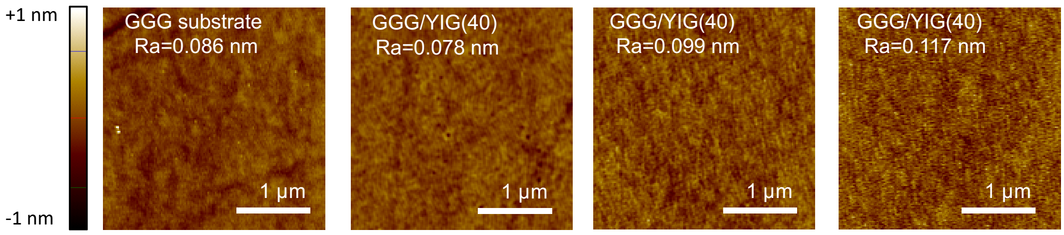

FIG.S2. AFM image of (a) GGG substrate, and (b-d) three randomly selected local areas of 40-nm thickness YIG films on the GGG substrate.

As shown in FIG.S2. (a), we have measured the AFM image of the GGG substrate used in our work, and it reveals a very smooth GGG surface with a roughness of 0.086 nm. To avoid chance, FIG.S2. (b-d) shows the AFM images for three randomly selected local areas of the YIG films (40 nm in thickness) with the average roughness of 0.078, 0.099, and 0.117 nm, respectively, indicating the smooth surfaces of the YIG films. The smooth morphology achieved in our YIG film can be attributed to the initial surface quality of the GGG substrate and the high-caliber epitaxial fabrication employed in creating the YIG/GGG heterostructure.

FIG.S3. (a) displays the hysteresis loop of the GGG/YIG sample under the in-plane magnetic field obtained by a Lake Shore vibrating sample magnetometer (VSM) at room temperature. Considering a 6-nm-thick magnetic dead layer at the interface [18], the GGG/YIG sample demonstrates a saturation magnetization of ~136 emu/cm^3, with a coercive field below 2 Oe, which agrees well with the previous work [19,20]. Fig. S3(b) shows the representative θ-2θ scan of the GGG/YIG heterostructure, demonstrating the purity of the YIG phase. According to the XRD spectra, the lattice constant of YIG film is 12.360 Å, which is close to the bulk lattice parameter (~12.376 Å). The appearance of Laue oscillations near the YIG (444) diffraction peak provides evidence of the film's exceptional flatness and uniformity.As shown in FIG.S3. (c) STEM and TEM images of the film indicate the high quality of our film, especially the YIG layer.

The left panel of FIG.S4.(a) shows the high-angle annular dark-field (HAADF) lattice image of the YIG layer on the GGG substrate collected by scanning transmission electron microscope (STEM) with double CS correctors, indicating the high-quality epitaxial growth of YIG. The right panel presents the cross-section of the YIG(40)/Pt(1.5)/Ru(5)/MgO(3)/Ta(2) stack, as captured by a high-resolution transmission electron microscopy (HR-TEM) (see S2 in the Supplemental Note for the overall cross-section of the full stack). The Ru layer and MgO layer also exhibit well-crystallized structures. FIG.S4.(b) showcases the corresponding energy dispersive spectroscopy (EDS) images, revealing the distribution of Y, Pt, Ru, and Mg elements. The interdiffusion of elements between different layers is minimal. The HR-TEM and EDS results validate the high quality of the sample and the sharp interfaces between the different layers.

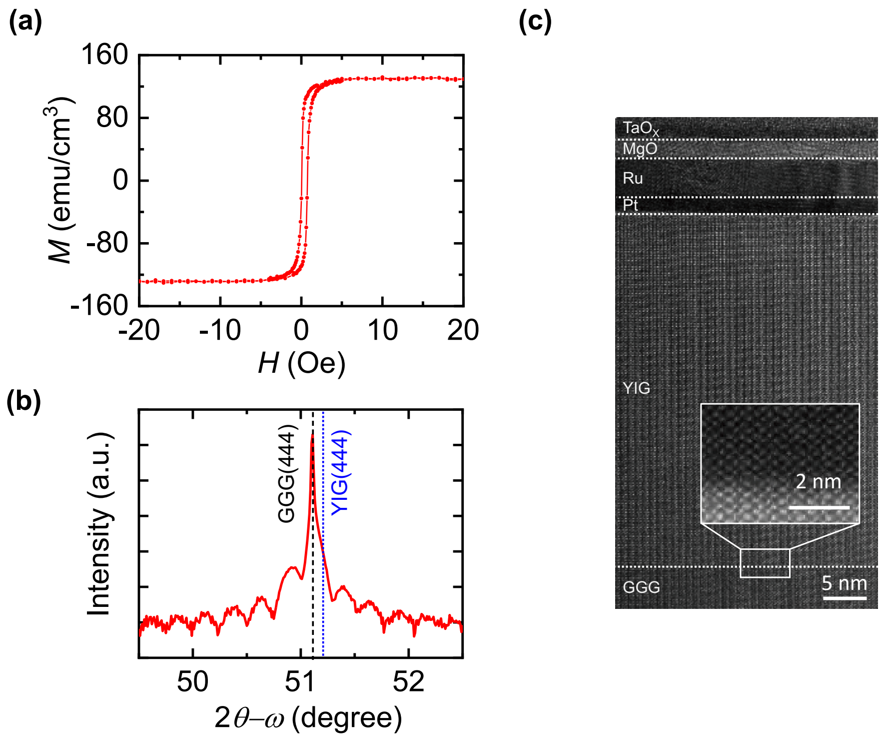

FIG.S3. (a) The magnetic loop of the GGG/YIG sample under the in-plane magnetic field. (b) XRD pattern of the GGG/YIG sample. (c)The overall cross-sectional HR-TEM image of the full stack, indicating the 40-nm thick YIG film on GGG is of high crystallinity and has no lattice relaxation. The inside shows HAADF-STEM image of the GGG/YIG interfaces.

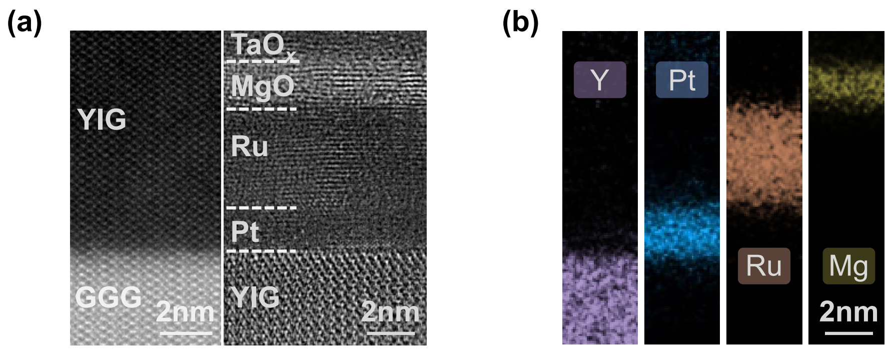

FIG.S4. Structural characterization of the sample. a) HAADF-STEM image of the GGG/YIG interface (left panel) and the cross-sectional HR-TEM image of the YIG(40)/Pt(1.5)/Ru(5)/MgO(3)/Ta(2) multilayer (right panel). b) The EDS mapping of corresponding elements.

S3. Thickness dependent SSE measurements in YIG(40)Pt(1.5)Ru(t_{Ru}) heterostructures

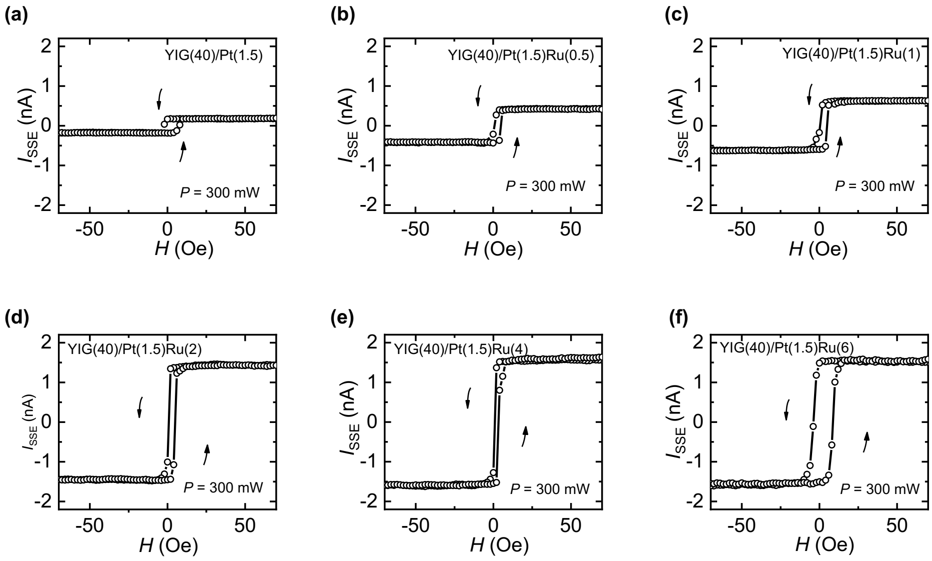

FIG.S5. SSE signals of YIG(40)Pt(1.5)Ru(t_{Ru}) with varying thicknesses of t_{Ru}.

S4. Thickness dependent SP measurements in YIG(40)Pt(1.5)Ru(t_{Ru}) heterostructures

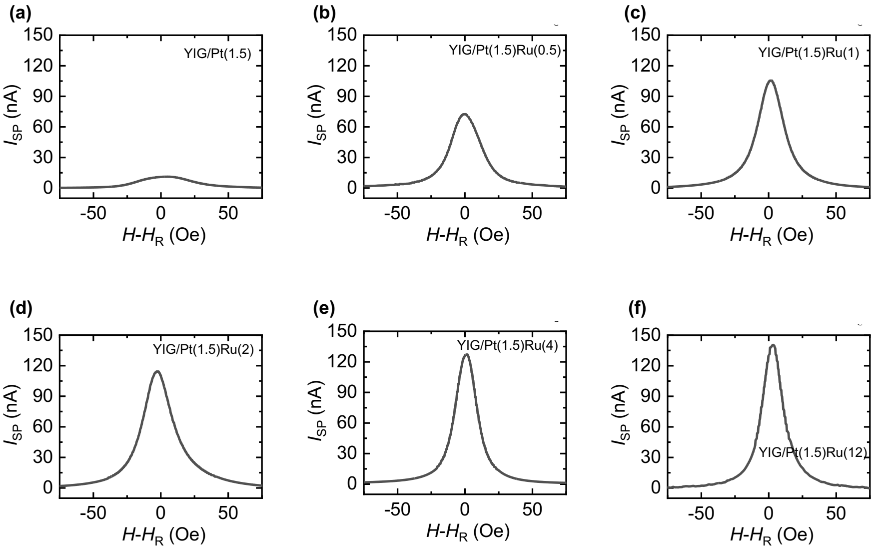

FIG.S6. SP signals of YIG(40)Pt(1.5)Ru(t_{Ru}) with varying thicknesses of t_{Ru}.

S5. The schematic of the spin sink and orbital sink effect

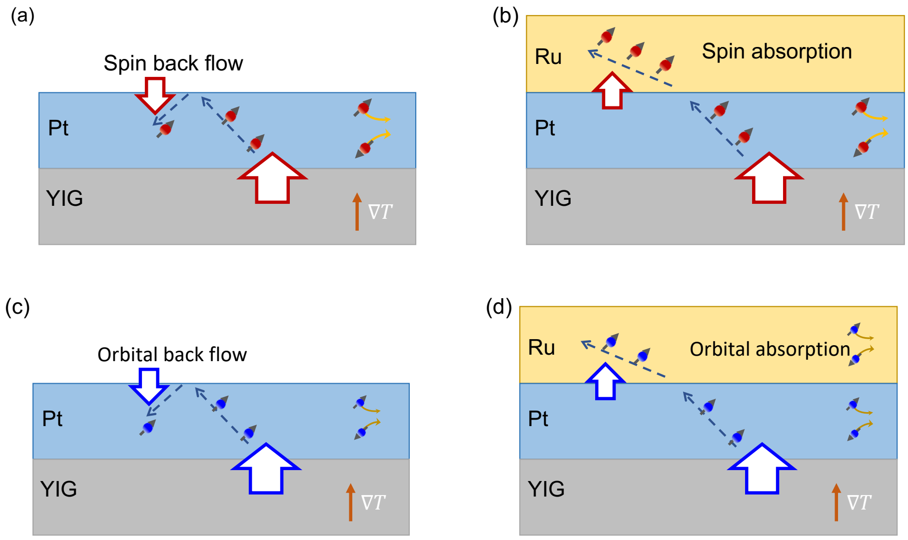

FIG.S7 (a) In a YIG/Pt structure, the polarized spin current from the YIG is partially reflected at the edge of the Pt layer. The spin backflow compensates the ISHE signal of Pt. (b) In a YIG/Pt/Ru structure, the spin reflection is constrained, thus boosting the spin-to-charge conversion in the Pt layer. (c) In a YIG/Pt structure, the polarized orbital current generated in the Pt layer is partially reflected at the Pt edge. The orbital backflow compensates the IOHE signal of Pt. (d) In a YIG/Pt/Ru structure, the Ru layer act as an orbital sink that constrains the orbital backflow, boosting the orbit-to-charge conversion in the Pt layer. the red (blue) arrows denote the spin (orbital) current.

Considering the spin scattering at a ferromagnet/Ru interface [13], we believe that in the YIG/Pt/Ru system, the spin-to-charge conversion could be enlarged by the spin scattering at the Pt/Ru interface. Notably, the enhancement of the SHE/ISHE signal from spin scattering is limited [14-16], which cannot well explain the increase of an order of magnitude increase in the SSE (SP) signal observed in our results. More importantly, spin scattering is an interfacial effect that occurs at the Pt/Ru interface. If this enhancement is dominated by interfacial spin scattering, a linear dependence of the enhanced signal on $1/t_{Ru}$ will be observed, which is a fingerprint of the interfacial effect. However, as shown in FIG.S8., the enhanced signals does not linearly grow as $1/t_{Ru}$ increases. After a careful analysis, we found that interfacial spin-dependent scattering may contribute to the enhancement of SSE and SP signals, but its impact is not the dominant factor.

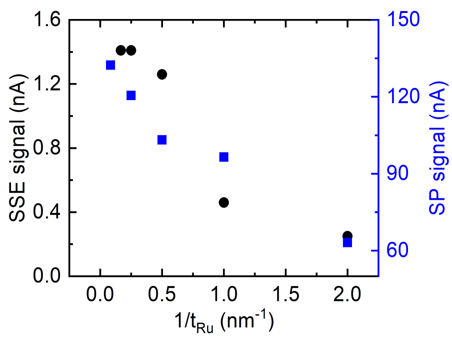

FIG.S8. SSE and SP signals of YIG/Pt/Ru samples as a function of the inverse thickness of the Ru layer.

S6. Estimate of the Joule heating in SSE and SP measurements

In the SSE measurements, Joule heating is intentionally generated in the resistance heater to establish a temperature gradient, which drives spin current generation in YIG. The injected spin current is then converted into a transverse electric signal in the adjacent metallic layers via ISHE and/or IOHE. The measured SSE signal is expressed as $I_{SSE}=V_{SSE}/R$, where R is the sample resistance measured after the temperature gradient is established. Since the electrical circuit used for SSE detection is fully separated from the heating circuit, Joule heating serves only to generate the temperature gradient and does not introduce an additional artifact into the measured SSE signal. Therefore, Joule heating does not affect the SSE results presented in the main text and Supplementary measurements.

In the SP measurements, Joule heating may in principle influence the bonding resistance and thereby affect the detected electrical signal. To evaluate this possibility, we varied the FMR input power from 7 to 10 dB. If Joule heating had a significant effect, the bonding resistance would change with increasing microwave power. However, the bonding resistance of the YIG/Pt/Ru sample remained nearly constant (~0.5345 Ω), indicating that the Joule heating effect on the electrical connection is negligible. In addition, the saturation magnetization of YIG extracted from the FMR absorption spectra was nearly independent of the applied microwave power (3, 5, and 7 dB). These results indicate that Joule heating has a negligible influence on the SP measurements reported in the main text and supplementary data.

S7. Experimental setup of SSE and SP measurements.

For the SSE measurements, the temperature gradient along the out-of-plane (z) direction was generated in a Quantum Design Physical Property Measurement System (PPMS) using the setup schematically illustrated in FIG.S9(a). The sample was sandwiched between a top copper block serving as a cold reservoir and a bottom copper plate attached to a resistive heater. The top copper block was thermally anchored to the PPMS sample chamber to stabilize the cold-side temperature, while the bottom heater provided a controlled heating power. Thermal grease was applied at all thermal interfaces to ensure good thermal contact and uniform heat flow. The entire assembly was mounted on a thermally insulating sample holder to promote quasi-one-dimensional heat transport.

The temperature difference ΔT across the sample was generated by resistive (Joule) heating of the bottom heater and calibrated experimentally using calibrated Pt100 resistance temperature sensors placed at the hot and cold reservoirs. As shown in FIG.S9(b), ΔT exhibits a linear dependence on the applied heating current, in agreement with previous calibration procedures reported in previous work [17].

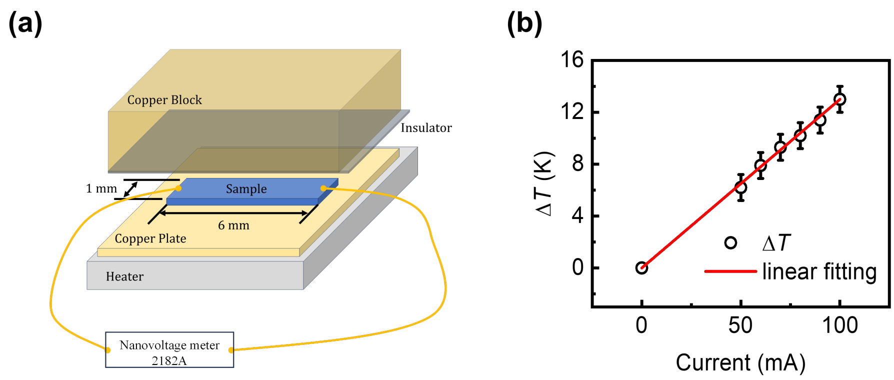

FIG.S9.(a) Schematic illustration of the experimental setup for the longitudinal spin Seebeck effect measurements. (b) Calibration of the temperature difference ΔT as a function of the applied heating current.

The spin pumping measurements were performed using the experimental configuration schematically shown in FIG.S10(a). A microwave signal generated by a vector network analyzer (Agilent N5230) was delivered to a stripline waveguide to produce a radio-frequency magnetic field for exciting ferromagnetic resonance (FMR) in the YIG layer. The output of the VNA was amplified by a microwave amplifier with a gain of 15 dB before being fed into the stripline. An external dc magnetic field was applied in the film plane and swept to establish the FMR condition. The inverse spin Hall voltage was detected using a Keithley 2182 nanovoltmeter.

To characterize the frequency-dependent microwave coupling and losses of the stripline device, the reflection coefficient S_{11} was measured using the VNA, as shown in FIG.S10(b). The S_{11} spectrum indicates that the insertion loss of the stripline waveguide is less than 0.6 dB over the frequency range used in this work, ensuring efficient microwave delivery to the sample.

The microwave excitation power was further examined by measuring the FMR absorption signal as a function of the input power at representative frequencies of 6, 7, and 8 GHz [Fig. FIG.S10(c)]. The approximately linear dependence of the absorption signal on the microwave power over the power range used in this work confirms that all spin pumping measurements were carried out within the linear excitation regime, excluding significant nonlinear or heating effects.

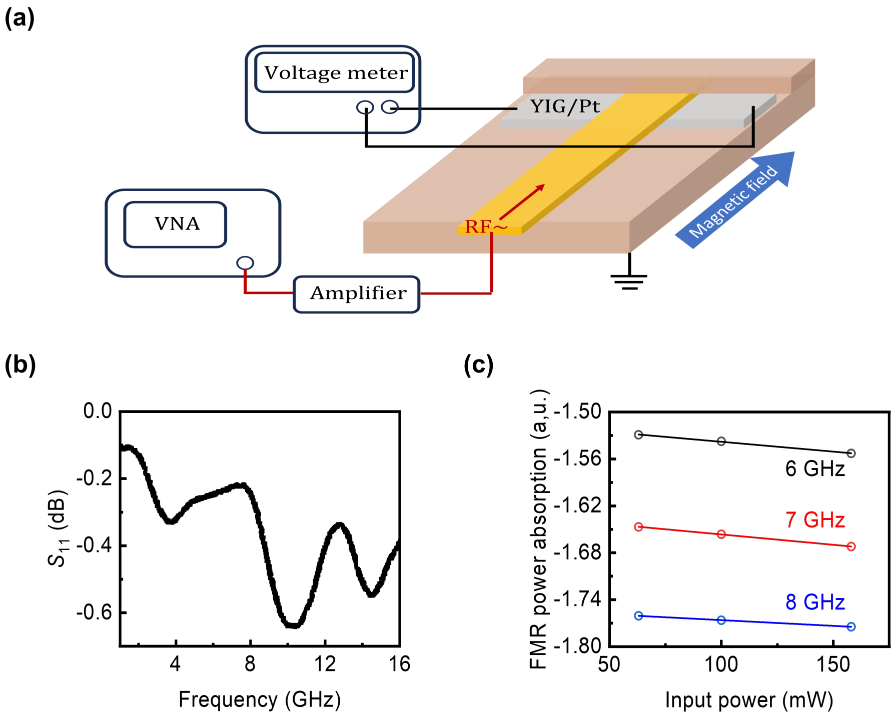

FIG.S10. (a) Schematic of the spin pumping measurement setup. (b) Frequency-dependent reflection coefficient S_{11} of the microwave line used for power calibration. (c) Microwave power dependence of the FMR absorption signal at 6, 7, and 8 GHz, confirming linear excitation conditions.

S8. SP and SSE measurements for YIG/Pt/NM structures with different NM layers.

To corroborate the hypothesis that the dominant factor responsible for signal enhancement is the IOHE, additional experiments were conducted involving other transition metals possessing large σ_{OH} [25]. We investigate the IOHE in the YIG/Pt(1.5)/NM(2) heterostructures (NM = Ta, W, Cu, and Ru) via both SSE and SP experiments, as shown in FIG.S11.(a) and (b). The results are ordered from weak to strong signals, and it is evident that the sample with the Ru layer exhibits the largest signal. On one hand, compared with heavy metals, Ru exhibits a very weak SOC, as indicated by the small spin Hall angle of 0.0056 and large spin diffusion length (about 5 nm) [26-28]. The negligible SHE/ISHE makes Ru an optimal candidate for studying OHE/IOHE. On the other hand, as a 4d transition metal Ru with an electronic configuration of $4d^7 5s^1$, the d band approximately achieves half-filling, fostering orbital hybridization within the energy band [10]. These could be the origin of the superiority of Ru with a very large OHC. Besides, the transmittance of the orbital current from the Pt layer into the NM layer is also an important factor, which could be impacted by interface engineering such as atomic disorder, lattice matching, and interfacial spin-orbit coupling (SOC)[22,24,29-32]. The largest signal observed in the YIG/Pt/Ru sample may benefit from the high orbital current transmittance at the Pt/Ru interface. At present, the exact contribution originating from the interface is challenging to ascertain from our present findings. It is worth noting that optimizing the orbital current transparency of the interface potentially could open a possibility for further improvement of the signal. In addition, FIG.S11.(a) and (b) also demonstrate the consistent agreement between SSE and SP measurements. Surprisingly, the signals of samples with NM = Ta and W also show a significant increase, which is inconsistent with the expectations based on ISHE alone. According to ISHE, the SSE and SP signals generated in Ta and W should partially cancel those from the Pt layer because the sign of their spin Hall conductivity (σ_{SH}) is opposite to that of Pt. In contrast, the orbital Hall conductivities (σ_{OH}) of Ta, W, and Pt share the same positive sign. This observation further supports the contribution of IOHE: the IOHE component overcomes the cancellation expected from ISHE in Ta and W, leading to an overall signal enhancement. Furthermore, the Cu sample—being a light metal and an inefficient spin sink (spin diffusion length exceeding 200 nm at room temperature [33])—also exhibits a substantial increase, further supporting that the spin sink effect plays only a minor role in our experiments. Unlike SHE/ISHE, which relies critically on the spin–orbit coupling of the electronic bands, OHE/IOHE is independent of the strength of spin–orbit coupling and can occur even without it. Various experimental works have reported evidence of OHE in metals with weak SOC by optical and transport measurements[34-37]. In our work, the strongest inverse orbital Hall effect is observed in materials where the spin-orbit coupling is weak because IOHE is mainly derived from orbital hybridization within the energy band, which is related to electron filling and atomic orbital mixing.

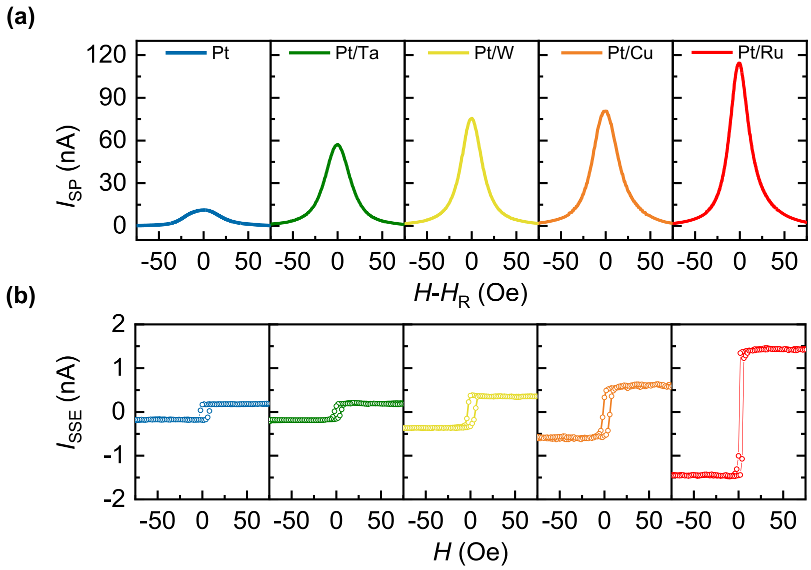

FIG.S11. SP and SSE measurements for different NM layers. a) SP measurements and b) SSE measurements of YIG/Pt/NM samples with various NM layers (Ta, W, Cu, and Ru).

References

[1] J. C. Rojas-Sánchez *et al.*, Spin Pumping and Inverse Spin Hall Effect in Platinum: The Essential Role of Spin-Memory Loss at Metallic Interfaces, Phys. Rev. Lett. **112**, 106602 (2014).

[2] J. Sinova, S. O. Valenzuela, J. Wunderlich, C. H. Back, and T. Jungwirth, Spin Hall effects, Rev. Mod. Phys. **87**, 1213 (2015).

[3] I. Žutić, J. Fabian, and S. Das Sarma, Spintronics: Fundamentals and applications, Rev. Mod. Phys. **76**, 323 (2004).

[4] J. Kim and Y. Otani, Orbital angular momentum for spintronics, J. Magn. Magn. Mater. **563**, 169974 (2022).

[5] R. Gupta *et al.*, Harnessing orbital Hall effect in spin-orbit torque MRAM, Nat. Commun. **16**, 130 (2025).

[6] D. Lee *et al.*, Orbital torque in magnetic bilayers, Nat. Commun. **12**, 6710 (2021).

[7] S. Ding *et al.*, Observation of the Orbital Rashba-Edelstein Magnetoresistance, Phys. Rev. Lett. **128**, 067201 (2022).

[8] S. Ding *et al.*, Harnessing Orbital-to-Spin Conversion of Interfacial Orbital Currents for Efficient Spin-Orbit Torques, Phys. Rev. Lett. **125**, 177201 (2020).

[9] G. Sala and P. Gambardella, Giant orbital Hall effect and orbital-to-spin conversion in 3 d, 5 d, and 4 f metallic heterostructures, Phys. Rev. Res. **4**, 033037 (2022).

[10] L. Salemi and P. M. Oppeneer, First-principles theory of intrinsic spin and orbital Hall and Nernst effects in metallic monoatomic crystals, Phys. Rev. Mater. **6**, 095001 (2022).

[11] X. Tao *et al.*, Self-consistent determination of spin Hall angle and spin diffusion length in Pt and Pd: The role of the interface spin loss, Sci. Adv. **4**, 1670 (2018).

[12] P. M. Haney, H.-W. Lee, K.-J. Lee, A. Manchon, and M. D. Stiles, Current induced torques and interfacial spin-orbit coupling: Semiclassical modeling, Phys. Rev. B. **87**, 174411 (2013).

[13] K.-W. Kim, Spin transparency for the interface of an ultrathin magnet within the spin dephasing length, Phys. Rev. B. **99**, 224415 (2019).

[14] H. Kontani, T. Tanaka, D. S. Hirashima, K. Yamada, and J. Inoue, Giant Orbital Hall Effect in Transition Metals: Origin of Large Spin and Anomalous Hall Effects, Phys. Rev. Lett. **102**, 016601 (2009).

[15] H. Yuasa, F. Nakata, R. Nakamura, and Y. Kurokawa, Spin Seebeck coefficient enhancement by using Ta50W50 alloy and YIG/Ru interface, J. Magn. Magn. Mater. **51**, 134002 (2018).

[16] S. Yakata, Y. Ando, T. Miyazaki, and S. Mizukami, Temperature dependences of spin-diffusion lengths of Cu and Ru layers, Jpn. J. Appl. Phys. **45**, 3892 (2006).

[17] V. Castel, N. Vlietstra, J. Ben Youssef, and B. J. van Wees, Platinum thickness dependence of the inverse spin-Hall voltage from spin pumping in a hybrid yttrium iron garnet/platinum system, Appl. Phys. Lett. **101**, 132414 (2012).

[18] A. Mitra *et al.*, Interfacial Origin of the Magnetisation Suppression of Thin Film Yttrium Iron Garnet, Sci. Rep. **7**, 11774 (2017).

[19] N. Sokolov *et al.*, Thin yttrium iron garnet films grown by pulsed laser deposition: Crystal structure, static, and dynamic magnetic properties, J. Appl. Phys. **119**, 023903 (2016).

[20] T. Liu *et al.*, Changes of Magnetism in a Magnetic Insulator due to Proximity to a Topological Insulator, Phys. Rev. Lett. **125**, 017204 (2020).

[21] I. Campbell and A. Fert, in *Transport properties of ferromagnets, Handbook of Ferromagnetic*

Materials Vol. 3 (Elsevier, The United Kingdom, 1982).
[22] Q. Bai, Y. Zhai, J. Yun, J. Zhang, M. Chang, Y. Zuo, and L. Xi, Highly efficient spin-current generation from Pt/Ru multilayers, Appl. Phys. Lett. **119**, 212404 (2021).
[23] H. Ju, X. Zhao, W. Liu, Y. Song, L. Liu, J. Ma, Y. Li, J. Wu, and Z. Zhang, Enhanced Spin–Orbit Torque and Low Critical Current Density in Pt100–x Ru x/[CoNi]/Ru Multilayer for Spintronic Devices, ACS Appl. Mater. Interfaces **13**, 61742 (2021).
[24] O. Gueckstock *et al.*, Terahertz Spin-to-Charge Conversion by Interfacial Skew Scattering in Metallic Bilayers, Adv. Mater. **33**, 2006281 (2021).
[25] D. Lee *et al.*, Orbital torque in magnetic bilayers, Nat. Commun. **12**, 6710 (2021).
[26] Z. Wen, J. Kim, H. Sukegawa, M. Hayashi, and S. Mitani, Spin-orbit torque in Cr/CoFeAl/MgO and Ru/CoFeAl/MgO epitaxial magnetic heterostructures, AIP Adv **6**, 056307 (2016).
[27] N. Behera, M. S. Singh, S. Chaudhary, D. K. Pandya, and P. Muduli, Effect of Ru thickness on spin pumping in Ru/Py bilayer, J. Appl. Phys. **117**, 17A714 (2015).
[28] C. Swindells, A. T. Hindmarch, A. J. Gallant, and D. Atkinson, Spin transport across the interface in ferromagnetic/nonmagnetic systems, Phys. Rev. B. **99**, 064406 (2019).
[29] W. Zhang, W. Han, X. Jiang, S.-H. Yang, and S. S. P. Parkin, Role of transparency of platinum-ferromagnet interfaces in determining the intrinsic magnitude of the spin Hall effect, Nat. Phys. **11**, 496 (2015).
[30] K. Gupta, R. J. H. Wesselink, R. Liu, Z. Yuan, and P. J. Kelly, Disorder Dependence of Interface Spin Memory Loss, Phys. Rev. Lett. **124**, 087702 (2020).
[31] I. Campbell and A. Fert, *Transport properties of ferromagnets, Handbook of Ferromagnetic Materials* (Elsevier, Elsevier, 1982), Vol. 3.
[32] H. Ju, X. Zhao, W. Liu, Y. Song, L. Liu, J. Ma, Y. Li, J. Wu, and Z. Zhang, Enhanced Spin–Orbit Torque and Low Critical Current Density in $Pt_{100-x}Ru_x$/[CoNi]/Ru Multilayer for Spintronic Devices, ACS Appl. Mater. Interfaces **13**, 61742 (2021).
[33] T. Kimura, T. Sato, and Y. Otani, Temperature Evolution of Spin Relaxation in a $\mathrm{NiFe}/\mathrm{Cu}$ Lateral Spin Valve, Phys. Rev. Lett. **100**, 066602 (2008).
[34] D. Go, D. Jo, C. Kim, and H.-W. Lee, Intrinsic Spin and Orbital Hall Effects from Orbital Texture, Phys. Rev. Lett. **121**, 086602 (2018).
[35] Y.-G. Choi *et al.*, Observation of the orbital Hall effect in a light metal Ti, Nature **619**, 52 (2023).
[36] I. Lyalin, S. Alikhah, M. Berritta, P. M. Oppeneer, and R. K. Kawakami, Magneto-Optical Detection of the Orbital Hall Effect in Chromium, Phys. Rev. Lett. **131**, 156702 (2023).
[37] S. Lee *et al.*, Efficient conversion of orbital Hall current to spin current for spin-orbit torque switching, Commun. Phys. **4**, 234 (2021).